CrossMark

The effect of Nb and Ni addition on crystallization behavior of amorphous–nanocrystalline Fe–Cr–B–Si alloys

Majid Tavoosi[1]

Abstract The crystallization behavior of amorphous Fe–Cr–B–Si alloys in the presence of Ni and Nb elements was the goal of this study. In this regard, four different amorphous–nanocrystalline $Fe_{40}Cr_{20}Si_{15}B_{15}M_{10}$ (M=Fe, Nb, Ni, $Ni_{0.5}Nb_{0.5}$) alloys were prepared using mechanical alloying technique up to 20 h. Based on the achieved results, in contrast to $Fe_{50}Cr_{20}Si_{15}B_{15}$ alloy, the amorphous phase can be successfully prepared in the presence of Ni and Nb in composition. Although the crystallization mechanism of prepared amorphous phase in different alloys was the same, the $Fe_{40}Cr_{20}Si_{15}B_{15}Nb_{10}$ alloy showed higher thermal stability in comparison with other samples. The crystallization activation energy of this amorphous alloy was estimated about 410 kJ mol^{-1} which was much higher than $Fe_{40}Cr_{20}Si_{15}B_{15}Ni_{10}$ (195.5 kJ mol^{-1}) and $Fe_{40}Cr_{20}Si_{15}B_{15}Ni_5Nb_5$ (360 kJ mol^{-1}) samples. The calculated values of Avrami exponent ($1.5 < n < 2.2$) indicated that the crystallization process in different alloying systems is the same and to be governed by a three-dimensional diffusion-controlled growth.

Keywords Fe-based · Amorphous–nanocrystalline alloys · Crystallization · Kinetic

✉ Majid Tavoosi
ma.tavoosi@gmail.com

1 Department of Materials Engineering, Malek-Ashtar University of Technology (MUT), Shahin Shahr, Iran

Introduction

Amorphous metallic alloys have been of interest in fundamental studies and potential applications for over 40 years. Amorphous structures have been made in many alloying systems and show a variety of unique properties, such as high yield strength, large elastic limit, high corrosion and were resistance, low elastic modulus and modified magnetic behavior, in comparison with their crystalline counterparts [1].

Fe-based system is attractive group of amorphous materials because of the low cost of iron, the relatively high strength and hardness [2–5] and excellent magnetic softness such as high saturation of magnetization, low coercivity (Hc) and low magnetic core loss [6]. Although this alloying system is of technological interest, its glass-forming ability is low and the formation of amorphous phase in this system is difficult. It has been shown that the glass-forming ability and the thermal stability of amorphous materials can be improved by the addition of one or more alloying elements to these systems [7–9]. Boron, Silicon, carbon and phosphorus are common alloying elements in Fe-based alloys. The addition of these elements to Fe-based alloys improves their ability to form amorphous as well as nanocrystalline phases. The Zr, Nb, Ga, Cr and Cu are other alloying elements that can be added to the composition to improve the glass-forming ability, thermal stability, magnetic and corrosion behaviors of Fe-based alloys. In this regards, the formation of amorphous Fe–Zr–B, Fe–Al–Ga–P–C–B, Fe–Si–B–Nb–Cu, Fe–Zr–B–Cu and Fe–Al–P–C–B alloys is noteworthy [1].

Although there have been numerous studies on the formation and characterization of amorphous and nanocrystalline phases in Fe–Cr–B–Si alloying system [3–5], the preparation and characterization of Fe–Cr–B–Si in the

presence of Ni and Nb elements have received relatively little attention. Thus, study about the exact effects of Ni and Nb elements on the formation and thermal stability of amorphous phase in this alloying system was the aim of this work. In this regard, the $Fe_{40}Cr_{20}Si_{15}B_{15}M_{10}$ (M=Fe, Nb, Ni, $Ni_{0.5}Nb_{0.5}$) amorphous alloys were prepared using mechanical alloying technique and the structural and phase changes during milling and annealing processes were evaluated. Moreover, the crystallization kinetic of these glasses was analyzed and values of the crystallization activation energy and Avrami exponent were established.

Experimental

The powders of Fe (99.9%), Cr (99%), B (99%), Si (99%), Ni (99.99%) and Nb (99.9%) were used as raw materials. The elemental powders with different compositions (based on Table 1) were mechanically alloyed in a planetary ball mill under an argon atmosphere. The mechanical alloying (MA) was performed in a steel container at room temperature. A rotation speed of 400 rpm and ball-to-powder ratio of 20:1 was employed. Annealing procedure had been done at temperature range of 850–1050 K (based on DSC results) for 2 h. Before annealing, the powder samples were sealed in a quartz tube under the vacuum of 10^{-3} Pa in order to prevent form oxidation during annealing.

X-ray diffractometery was used to follow the structural changes of the powders during the milling and subsequence annealing. A Philips diffractometer (40 kV) with Cu Ka radiation ($k = 0.15406$ nm) was used for the XRD measurements. The XRD patterns were recorded in the 2θ range of 10°–80° (step size 0.03°; time per step 1 s). The microstructure of the produced amorphous–nanocrystalline samples were investigated using a transmission electron microscopy (TEM, Jeol-JEM-3010). The differential thermal analysis was also conducted to study the thermal stability of the produced amorphous alloys using a Reometric STA 1500 differential thermal analyzer. The samples were placed in Al_2O_3 pans and heated in a dynamic argon atmosphere up to 1270 K at different heating rates of 10, 20 and 30 K min^{-1}.

Table 1 Atomic percentages of Fe, Cr, B, Si, Ni and Nb elements in different samples

S.N.	Element content/at.%					
	Fe	Cr	B	Si	Ni	Nb
1	50	20	15	15	–	–
2	40	20	15	15	10	–
3	40	20	15	15	5	5
4	40	20	15	15	–	10

Results and discussion

The XRD patterns of the $Fe_{50}Cr_{20}Si_{15}B_{15}$ powder mixture after various milling processing periods are shown in Fig. 1. In the early stage of the MA process, only the broadening of alloying elements peaks accompanied by remarkable decreases in their intensities occurred as a result of the refinement of the crystalline sizes and increments of the lattice strains. Increasing milling time to 5 h led to the disappearance of the Cr, B and Si peaks, while the Fe peaks shifted to higher angles. This can be related to the dissolution of these elements in Fe lattice and formation of Fe–Cr–B–Si solid solution. In fact, increasing the density of crystalline defects such as phase and grain boundaries, dislocations and vacancies is the main reason for the formation of Fe solid solution during mechanical alloying [2]. The results shows that, by milling the powder mixture up to 20 h, gradual grain refinement is the only considerable change that occurs in the powder mixture, and the crystallite size reaches to a constant value of about 20 nm (based on presented TEM image in Fig. 2).

The presented results showed that the glass-forming ability of $Fe_{50}Cr_{20}Si_{15}B_{15}$ is low and amorphous phase cannot be formed in this alloy during milling up to 20 h. Formation of amorphous phase during mechanical alloying process occurs by an interdiffusion reaction along constituent interfaces at relatively low temperature. The formation of amorphous phase in this technique depends on the milling parameters and thermodynamic properties of the alloying system [1]. In fact, milling parameters, such as rotation speed, ball-to-powder ratio, the size and distribution of balls, milling temperature and time, can influence the structure of the mechanically milled alloys [8, 9].

Although the formation of amorphous phase may be possible by slight variation in these processing parameters, in the present study, all of these parameters were kept
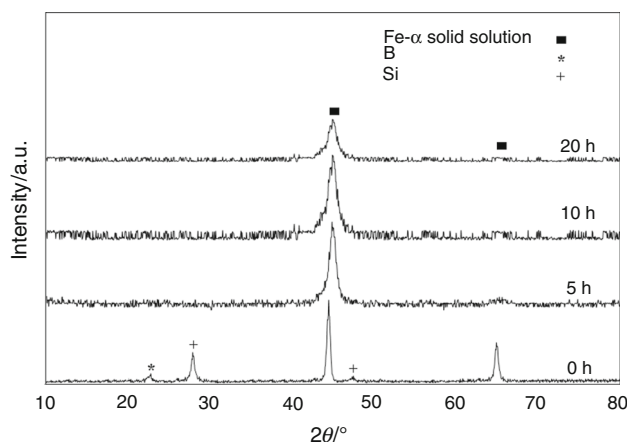

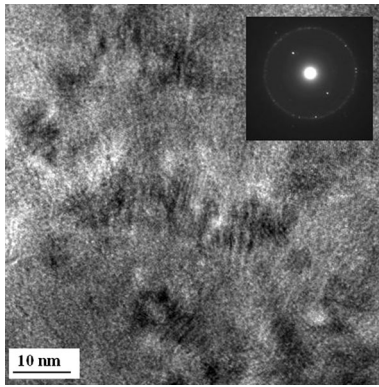**Fig. 1** XRD patterns of the $Fe_{50}Cr_{20}Si_{15}B_{15}$ powder mixture milled for different periods of time

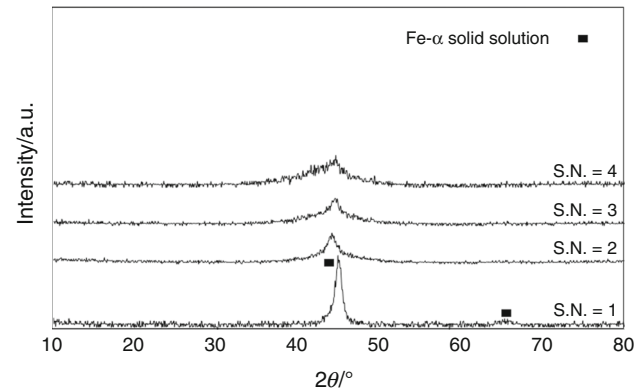**Fig. 2** TEM micrograph of $Fe_{50}Cr_{20}Si_{15}B_{15}$ powder mixture after 20 h of milling

Fig. 3 XRD patterns of the $Fe_{40}Cr_{20}Si_{15}B_{15}M_{10}$ (M=Fe, Nb, Ni, $Ni_{0.5}Nb_{0.5}$) powder mixtures after 20 h of milling

constant and the effect of Ni and Nb elements, with two different amounts of heat of solution in Fe matrix, on the formation of amorphous phase in Fe–Cr–Si–B alloying system was investigated. In fact, the solution heat of Nb in Fe (about -72 kJ mol^{-1}) is much higher than the solution heat of Ni in Fe (-9 kJ mol^{-1}) matrix. By attention to this point, the effect of Nb on glass-forming ability and thermal stability of formed amorphous phase is higher than Ni element. In this regard, milling process has been performed in $Fe_{40}Cr_{20}Si_{15}B_{15}M_{10}$ (M=Fe, Nb, Ni, $Ni_{0.5}Nb_{0.5}$) powder mixture at same condition and the structure of prepared samples was examined using XRD technique. The XRD patterns of prepared samples after 20 h of milling are presented in Fig. 3. As seen, in contrast to $Fe_{50}Cr_{20}Si_{15}B_{15}$ alloy (S.N. = 1), the X-ray patterns of $Fe_{40}Cr_{20}Si_{15}B_{15}Ni_{10}$ (S.N. = 2), $Fe_{40}Cr_{20}Si_{15}B_{15}Ni_5Nb_5$ (S.N. = 3) and $Fe_{40}Cr_{20}Si_{15}B_{15}Nb_{10}$ (S.N. = 4) alloys exhibit one broad diffuse scattering halo (in 2θ range of 40°–50°) and some crystallization peaks (corresponding to Fe-based solid solution) with low strength confirming that the microstructure of the samples is not fully amorphous. This result is in agreement with the TEM micrograph of $Fe_{40}Cr_{20}Si_{15}B_{15}Ni_{10}$ as-milled sample which is presented in Fig. 4. Based on this micrograph, there are evidences of nanocrystalline phases in the structure of this sample and this specimen is not fully amorphous.

The formation mechanism of amorphous phase during milling process is attributed to the microstructural breakdown followed by interdiffusion of elements or mechanically driven atomic mixing among previously formed nanocrystalline multilayer. The transformation of Fe-α solid solution to amorphous structure during MA is believed to occur as a result of the internal energy increase
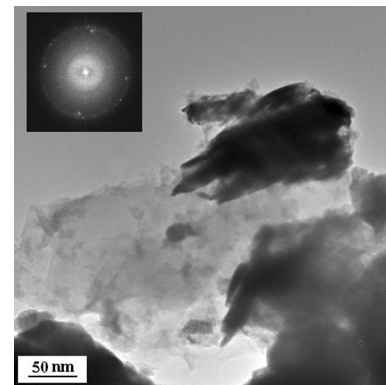

Fig. 4 TEM micrograph of $Fe_{40}Cr_{20}Si_{15}B_{15}Nb_{10}$ powder mixture after 20 h of milling

of the crystalline structure due to the creation of a high density of lattice defects as well as the dissolution of a great amount of solute atoms with different sizes in Fe lattice. When the free energy of the crystalline solid solution exceeds the free energy of the amorphous state, the crystalline structure thermodynamically becomes unstable and transforms to the amorphous structure [1].

The amorphous phase is in a metastable state, and considerable structural and phase changes can occur upon heating. In order to study the effect of Ni and Nb elements on thermal stability of the prepared amorphous phases, the samples were examined using DSC technique under continuous heating conditions. The DSC heating traces of in $Fe_{40}Cr_{20}Si_{15}B_{15}Ni_{10}$, $Fe_{40}Cr_{20}Si_{15}B_{15}Ni_5Nb_5$ and $Fe_{40}Cr_{20}Si_{15}B_{15}Nb_{10}$ alloying systems at different heating rates are presented in Figs. 5–7, respectively. Different characteristic temperatures such as glass transition temperature (T_g), crystallization temperature (T_x), peak of
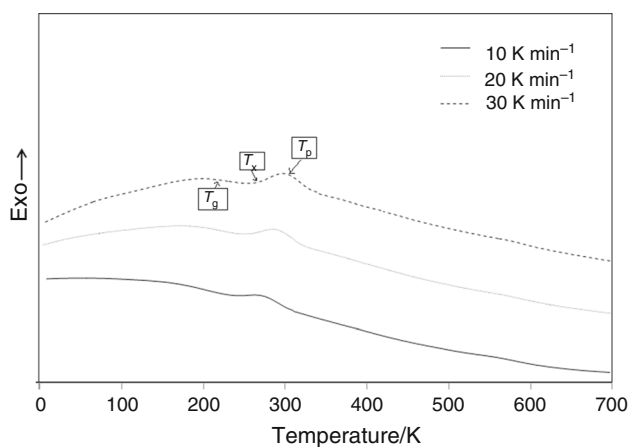
Fig. 5 DSC heating traces of $Fe_{40}Cr_{20}Si_{15}B_{15}Ni_{10}$ amorphous phase at different heating rates of 10–30 K min^{-1}

Fig. 6 DSC heating traces of $Fe_{40}Cr_{20}Si_{15}B_{15}Ni_5Nb_5$ amorphous phase at different heating rates of 10–30 K min^{-1}

Fig. 7 DSC heating traces of $Fe_{40}Cr_{20}Si_{15}B_{15}Nb_{10}$ amorphous phase at different heating rates of 10–30 K min^{-1}
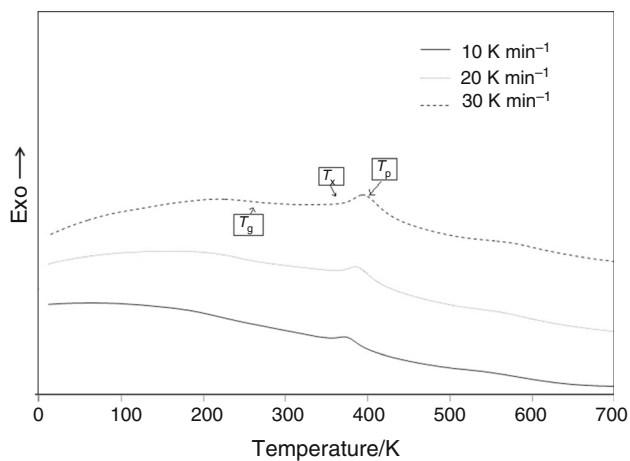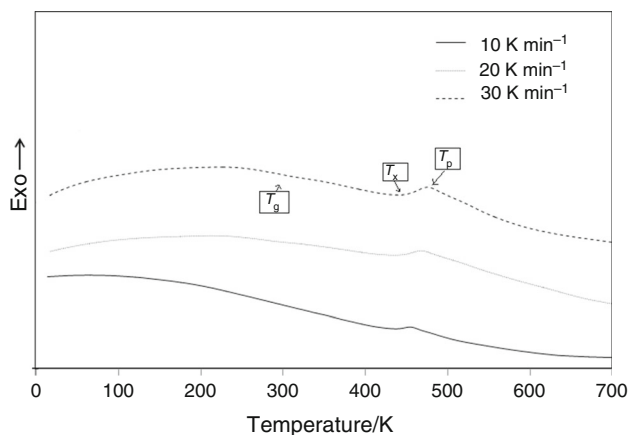
Table 2 Crystallization temperature, products and sequence of $Fe_{40}Cr_{20}Si_{15}B_{15}Ni_{10}$, $Fe_{40}Cr_{20}Si_{15}B_{15}Ni_5Nb_5$ and $Fe_{40}Cr_{20}Si_{15}B_{15}Nb_{10}$ amorphous alloys

S.N.	Characteristic temperature/K			Crystallization	
	T_g	T_x	T_p	products	sequence
2	783	833	857	Fe-α, FeB, Ni$_3$B, Ni$_2$Si	One stage
3	803	938	946	Fe-α, FeB, Nb$_5$B$_6$, Nb$_5$Si$_3$	One stage
4	848	1013	1038	Fe-α, FeB, Nb$_5$B$_6$, Nb$_5$Si$_3$	One stage

crystallization temperature (T_p) and crystallization parameters of prepared amorphous phases are also presented in Table 2. As seen, these curves are similar (each amorphous phase shows one-stage crystallization on heating) and only one exothermic peak appears in each DSC curve. To analyze the crystallization process responsible for this exothermic peak, the prepared amorphous samples were annealed in an argon atmosphere at the crystallization temperature for 2 h. The XRD pattern of the $Fe_{40}Cr_{20}Si_{15}B_{15}Ni_{10}$ amorphous phase after annealing at 875 K for 2 h is shown in Fig. 8a. As seen, this sample is composed of the Fe-α, FeB, Ni$_3$B, Ni$_2$Si phases. Therefore, the

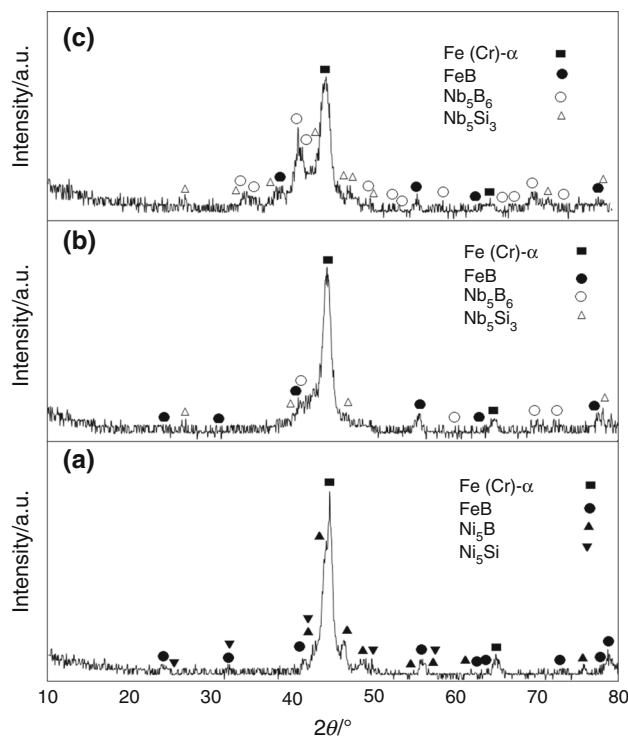**Fig. 8** XRD patterns of **a** $Fe_{40}Cr_{20}Si_{15}B_{15}Ni_{10}$ amorphous phase after annealing at 857 K for 2 h, **b** $Fe_{40}Cr_{20}Si_{15}B_{15}Ni_5Nb_5$ after annealing at 946 K for 2 h, **c** $Fe_{40}Cr_{20}Si_{15}B_{15}Nb_{10}$ after annealing at 1038 K for 2 h

exothermic peak in Fig. 5 should be attributed to the precipitation of the Fe-α and FeB, Ni_3B, Ni_2Si phases from the amorphous matrix (amorphous → Fe + FeB + Ni_3B + Ni_2Si).

The similar analysis was also performed for $Fe_{40}Cr_{20}Si_{15}B_{15}Ni_5Nb_5$ and $Fe_{40}Cr_{20}Si_{15}B_{15}Nb_{10}$ amorphous phase, and the results are presented in Fig. 8 and Table 2. According to these results, the total crystallization sequences of the $Fe_{40}Cr_{20}Si_{15}B_{15}Ni_{10}$, $Fe_{40}Cr_{20}Si_{15}B_{15}Ni_5Nb_5$ and $Fe_{40}Cr_{20}Si_{15}B_{15}Nb_{10}$ amorphous alloys are similar (one-stage crystallization processes), but the crystallization products and temperatures in these three systems differ from each other. The crystallization products in the $Fe_{40}Cr_{20}Si_{15}B_{15}Ni_5Nb_5$ and $Fe_{40}Cr_{20}Si_{15}B_{15}Nb_{10}$ alloying systems are Fe-α, FeB, Nb_5B_6 and Nb_5Si_3 phases which are different from the crystallization phases in the $Fe_{40}Cr_{20}Si_{15}B_{15}Ni_{10}$ alloy. Moreover, the crystallization temperatures of the $Fe_{40}Cr_{20}Si_{15}B_{15}Ni_{10}$, $Fe_{40}Cr_{20}Si_{15}B_{15}Ni_5Nb_5$ and $Fe_{40}Cr_{20}Si_{15}B_{15}Nb_{10}$ amorphous alloys are estimated about 857, 946 and 1038 K, respectively. This result illustrates that the thermal stability of amorphous phase in $Fe_{40}Cr_{20}Si_{15}B_{15}Nb_{10}$ alloy is much higher than two other systems.

The crystallization activation energy, Avrami exponent and frequency factor are three main parameters for describing the crystallization kinetics of amorphous materials. In calorimetric measurements, non-isothermal methods can be used to calculate these parameters. The theoretical basis for interpreting thermal analysis data for crystallization of amorphous phase is provided by the classical Johnson–Mehl–Avrami (JMA) model. In this model, the volume fraction of crystallization (α) can be expressed as a function of time according to the following relation [10]:

$$\alpha(t) = 1 - \exp[-Kt^n] \qquad (1)$$

where K and n are the effective overall reaction rate constant and Avrami exponent, respectively. The effective overall reaction rate constant (K) usually has Arrhenius temperature dependence as follow:

$$K = K_0 \exp(-E/RT_P) \qquad (2)$$

In this equation, K_0 is the frequency factor, T is temperature and E is the activation energy describing the overall crystallization process. Kissinger's equation [11] using the non-isothermal DSC measurement can be used to estimate the effective activation energy of the crystallization:

$$\ln(\beta/T_P^2) = (E/T_P) + \text{constant} \qquad (3)$$

where T_P is the related temperature to the maximum point of exothermic peak, β is the heating rate, R is the gas constant and E is the crystallization activation energy.

Kissinger's plot $\ln(\beta/T_P^2)$ versus $1/T$ results in approximately straight lines. Based on the slope of Kissinger's plots of $Fe_{40}Cr_{20}Si_{15}B_{15}Ni_{10}$, $Fe_{40}Cr_{20}Si_{15}B_{15}Ni_5Nb_5$ and $Fe_{40}Cr_{20}Si_{15}B_{15}Nb_{10}$ amorphous alloys (Fig. 9), the effective activation energy of the crystallization of different samples was estimated and the results are given in Table 3. As seen, the crystallization activation energy of amorphous phase in different alloys decrease in the order of $Fe_{40}Cr_{20}Si_{15}B_{15}Nb_{10}$ (405.5 kJ mol^{-1}) > $Fe_{40}Cr_{20}Si_{15}B_{15}Ni_5Nb_5$ (360 kJ mol^{-1}) > $Fe_{40}Cr_{20}Si_{15}B_{15}Ni_{10}$ (195.5 kJ mol^{-1}). This result also confirms that $Fe_{40}Cr_{20}Si_{15}B_{15}Nb_{10}$ amorphous alloy has higher thermal stability in comparison with two other samples. This behavior can be related to the higher heat of solution of Nb in Fe matrix in comparison with Ni. However, the activation energy is quite high, much smaller than the energies measured for the good glass formers in Zr-based [12], $[(Fe_{0.5}Co_{0.5})_{0.75}B_{0.20}Si_{0.05}]_{96}Nb_4$ and $[(Fe_{0.6}Co_{0.3}Ni_{0.1})_{0.75}\ B_{0.2}Si_{\ 0.05}]_{96}Nb_4$ alloys (more than 550 kJ mol^{-1}) [13, 14].

It is important to note that besides above-mentioned models which are commonly used in the glass community including this study, many other methods with different
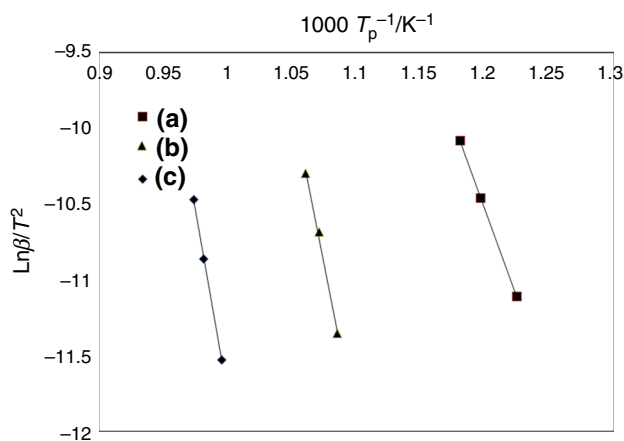

Fig. 9 Kissinger's plot of $\ln(\beta/T_P^2)$ versus $1000/T$ for crystallization of **a** $Fe_{40}Cr_{20}Si_{15}B_{15}Ni_{10}$, **b** $Fe_{40}Cr_{20}Si_{15}B_{15}Ni_5Nb_5$ and **c** $Fe_{40}Cr_{20}Si_{15}B_{15}Nb_{10}$ amorphous alloys

Table 3 Different crystallization parameters of $Fe_{40}Cr_{20}Si_{15}B_{15}Ni_{10}$, $Fe_{40}Cr_{20}Si_{15}B_{15}Ni_5Nb_5$ and $Fe_{40}Cr_{20}Si_{15}B_{15}Nb_{10}$ amorphous phases

S.N.	Activation energy/ kJ mol^{-1}	Avrami exponent	Nucleation index (a)	Growth index (c)	Growth dimension (b)
2	195.5	1.8–2.18	0 < a < 1	0.5	3
3	360	1.7–1.9	0 < a < 1	0.5	3
4	405.5	1.56–1.7	0 < a < 1	0.5	3

derivatives have been also proposed by Piloyan–Borchardt [15], Coats–Redfern [16], Šesták [17] and Ligero et al. [18]. While all of these methods are based on the Johnson–Mehl–Avrami theory, they differ greatly in their assumption; in some cases, they may lead to contradictory results. Therefore, controversy exists in using these models and ultimate care should be devoted. Moreover, in presented models, the surface crystallization process has been ignored [18] and the Avrami exponent which is valid for isothermal conditions extends to the transformation under non-isothermal conditions. In fact, this work imposes further complications of the theoretical interpretation of the kinetic results [19].

The total amount of crystallization can be directly attributed to the area under the DSC curve. By attention to this point, the crystallization volume fraction of amorphous phase, α, as a function of temperature, T, can be obtained from the DSC curves. The crystallized volume fraction, α, at any temperature T is given as $\alpha = (A_T/A)$. In this relation, A is the total area of the exothermic peak (between the temperature where the crystallization begins, T_i, and the temperature where the crystallization is completed, T_f) and A_T is the area between the initial temperature and any temperature T (between T_i and T_f). The plots of α versus T at different heating rates are shown in Fig. 10. As seen, the shapes of these plots are typical sigmoidal shapes, which appear frequently in the literature [20–22]. These sigmoidal plots show a slow initial period (incubation time). The rate of crystallization then increases mainly as a result of growth of nuclei and then again decreases due to the impingement of crystallites [22].

The local crystallization activation energy (as a function of crystallization fraction) can be determined using the Flynn–Wall–Ozawa method [23, 24]:

$$\log \beta = \log \frac{AE(\alpha)}{Rg(\alpha)} - 0.457 \frac{E(\alpha)}{RT} - 2.315 \qquad (4)$$

In this equation, A is the pre-exponential factor, $E(\alpha)$ is the local crystallization activation energy and $g(\alpha)$ is a function determined by the crystallization fraction. In fact,
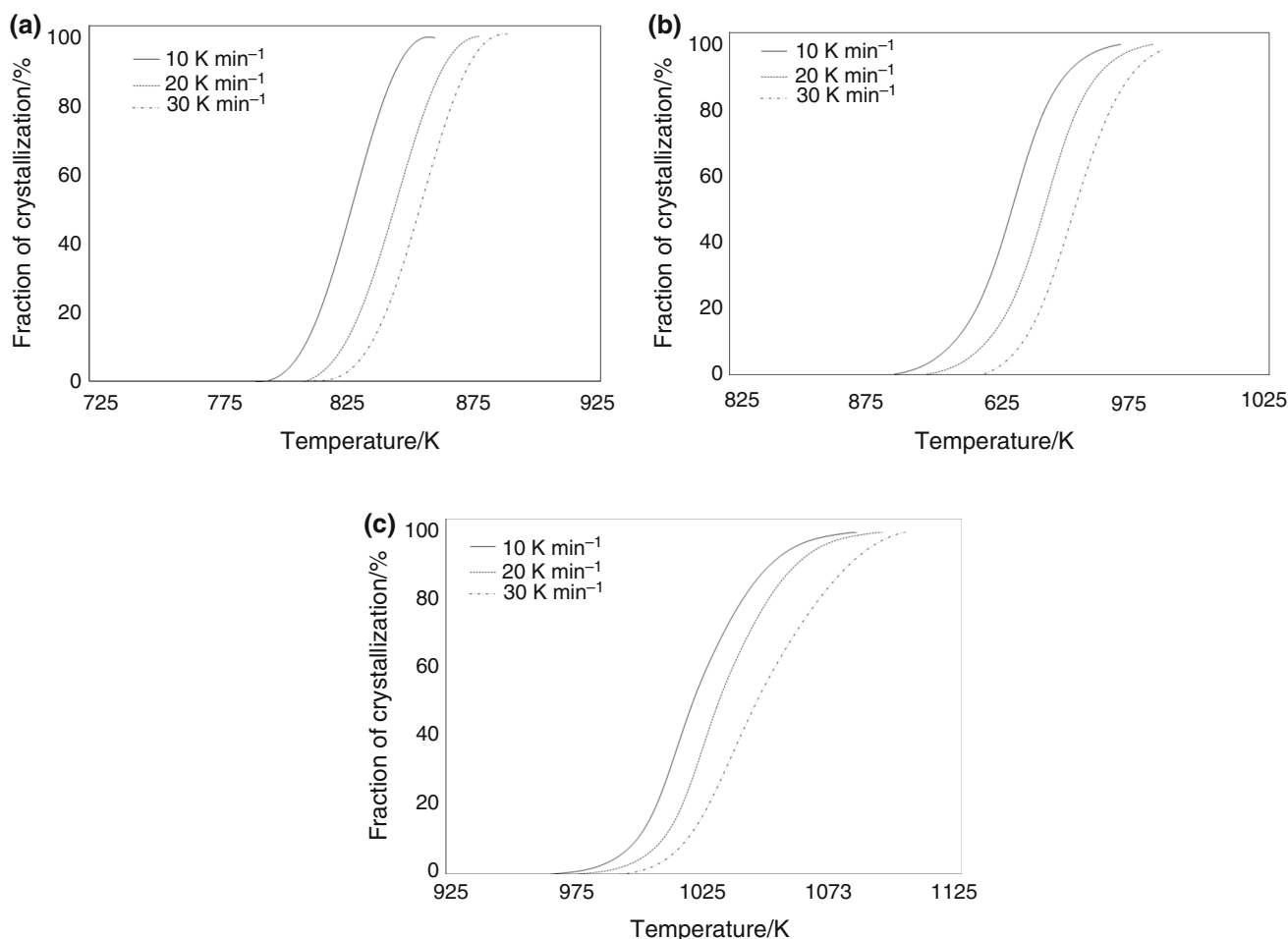

Fig. 10 Relationship between the crystallization fraction (α) and temperature (T) of **a** $\alpha Fe_{40}Cr_{20}Si_{15}B_{15}Ni_{10}$, **b** $Fe_{40}Cr_{20}Si_{15}B_{15}Ni_5Nb_5$ and **c** $Fe_{40}Cr_{20}Si_{15}B_{15}Nb_{10}$ amorphous alloys

a plot of $\log \beta$ versus $1000/T$ for the given values of the crystallization fraction gives the local activation energy of the crystallization. This method is employed to estimate the local activation energy of $Fe_{40}Cr_{20}Si_{15}B_{15}Ni_{10}$, $Fe_{40}Cr_{20}Si_{15}B_{15}Ni_5Nb_5$ and $Fe_{40}Cr_{20}Si_{15}B_{15}Nb_{10}$ amorphous alloys, and the final results are shown in Fig. 11. It can be seen that the overall crystallization activation energy of $Fe_{40}Cr_{20}Si_{15}B_{15}Nb_{10}$ amorphous alloy is higher than two other samples. Regardless of the chemical composition, the local activation energy of crystallization increases slightly with the progress of crystallization. This point indicates that the crystallization process becomes more difficult as the crystallization fraction increases.

The crystallization kinetics can be determined using the DSC and fitting the data with the Johnson–Mehl–Avrami (JMA) model as noted by Ozawa [25]:

$$\ln[-\ln(1-\alpha)] = -n\ln(\beta) + \ln X(T) \qquad (5)$$

where n is the Avrami exponent. The following formula was obtained after the transformation of Eq. (5) at a constant temperature T:

$$\left.\frac{d\{\ln[-\ln(1-\alpha)]\}}{d\ln\beta}\right|_T = -n \qquad (6)$$

The Avrami exponent of prepared amorphous phases were determined from the $\ln[-\ln(1-\alpha)]$ versus $\ln\beta$ plot, and the results are given in Table 3. As can be seen, the Avrami exponent for different samples is in the range of $1.5 < n < 2.2$. In this condition, the lowest amount of Avrami exponent can be related to $Fe_{40}Cr_{20}Si_{15}B_{15}Nb_{10}$ amorphous alloy which is in conferment with other results about more thermal stability of this alloy.

The Avrami exponent provides detailed information of the nucleation and growth mechanisms. Ranganathan and Heimendahl [26] suggested that this exponent can be expressed as:

$$n = a + bc \qquad (7)$$

where a is the nucleation index, which can range from 0 to 1 ($a = 0$ for a nucleation rate of zero, $0 < a < 1$ for a nucleation rate decreasing with time, $a = 1$ for a constant nucleation rate and $a > 1$ for an increasing nucleation
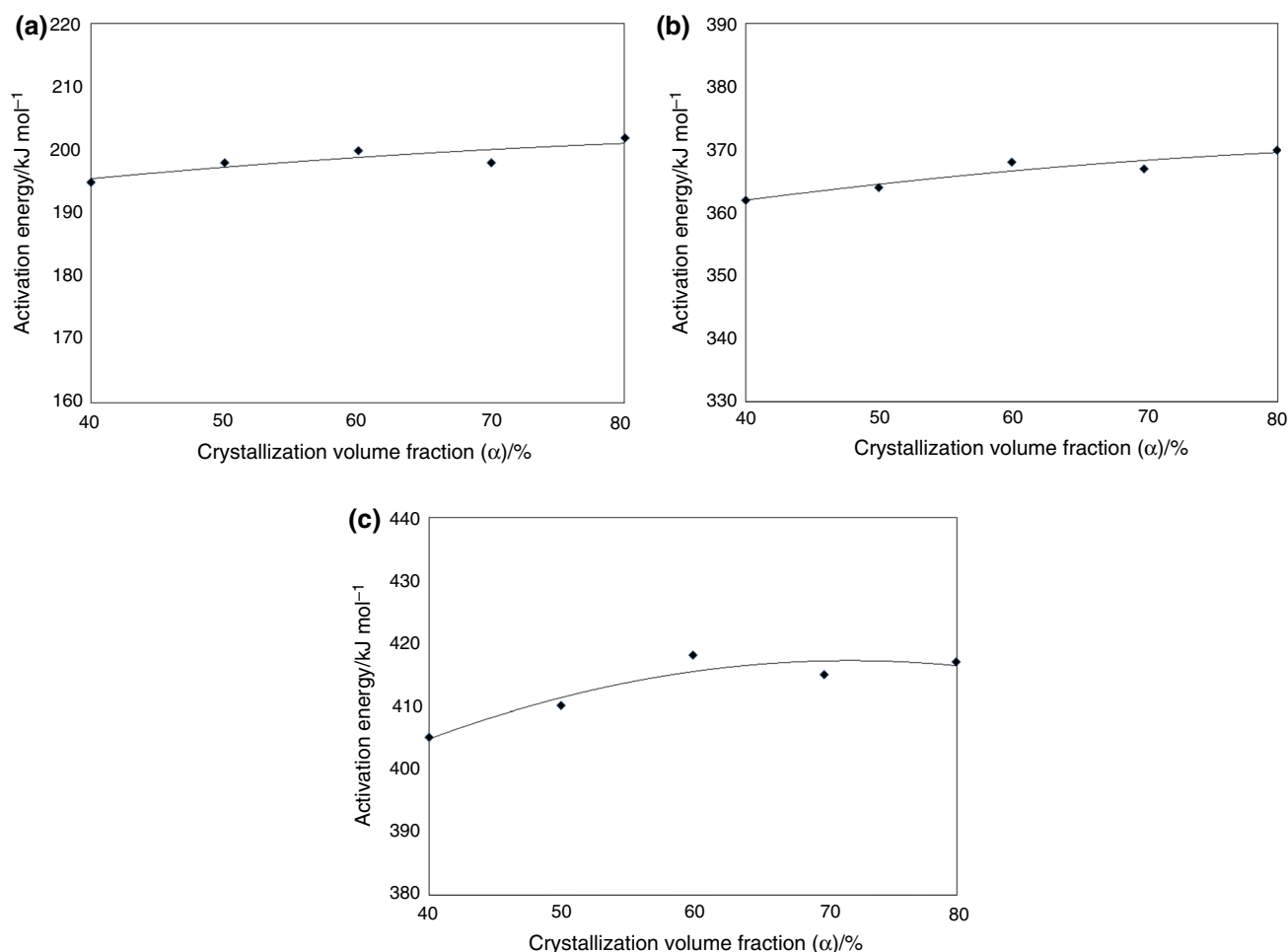

Fig. 11 Local crystallization activation energies versus the crystallization fraction of **a** $Fe_{40}Cr_{20}Si_{15}B_{15}Ni_{10}$, **b** $Fe_{40}Cr_{20}Si_{15}B_{15}Ni_5Nb_5$ and **c** $Fe_{40}Cr_{20}Si_{15}B_{15}Nb_{10}$ amorphous alloys

rate), b is the dimension of the growth (with values 1, 2 or 3 for one-, two- and three-dimensional growth, respectively) and c is the growth index ($c = 1$ for interface-controlled growth and $c = 0.5$ for diffusion-controlled growth). Based on above, the value of index a, b and c for crystallization of $Fe_{40}Cr_{20}Si_{15}B_{15}Ni_{10}$, $Fe_{40}Cr_{20}Si_{15}B_{15}Ni_5Nb_5$ and $Fe_{40}Cr_{20}Si_{15}B_{15}Nb_{10}$ amorphous alloys were estimated and the results are presented in Table 3. According to this table, regardless of the chemical composition, the crystallization of prepared amorphous phases in this study occurred with a decreasing nucleation rate and was governed by a three-dimensional diffusion-controlled growth.

Conclusions

From the investigation of structural and thermal characterization of amorphous-nanocrystalline Fe–Cr–B–Si–Ni–Nb alloys during milling and annealing processes, the following conclusions can be made:

1. In contrast to $Fe_{50}Cr_{20}Si_{15}B_{15}$ alloy, the amorphous phase can successfully prepare in presence of Ni and Nb in composition.
2. Although the crystallization mechanism (one-stage crystallization on heating) of prepared amorphous phases was the same, the alloys consisting of Nb element showed higher thermal stability in comparison with other samples.
3. The crystallization activation energy of $Fe_{40}Cr_{20}Si_{15}B_{15}Nb_{10}$ was estimated about 405.5 kJ mol^{-1} which was much higher than $Fe_{40}Cr_{20}Si_{15}B_{15}Ni_{10}$ (195.5 kJ mol^{-1}) and $Fe_{40}Cr_{20}Si_{15}B_{15}Ni_5Nb_5$ (360 kJ mol^{-1}) alloys.
4. The calculated values of Avrami exponent ($1.5 < n < 2.2$) indicated that the crystallization process in different alloying systems are the same and to be governed by a three-dimensional diffusion-controlled growth.

References

1. Inoue A, Hashimoto K. Amorphous and nanocrystalline materials: preparation, properties, and applications. New York: Springer; 2001.
2. Movahedi B, Enayati MH, Wong CC. Study on nanocrystallization and amorphization in F–Cr–Mo–B–P–Si–C system during mechanical alloying. Mater Sci Eng B. 2010;172:50–4.
3. Sunol JJ, Clavaguera N, Cavaguera-Mora MT. Comparison of Fe–Ni–P–Si alloys prepared by ball milling. J Non Cryst Solids. 2001;287:114–9.
4. Chen QJ, Fan HB, Shen J, Sun JF, Lu ZP. Critical cooling rate and thermal stability of Fe–Co–Zr–Y–Cr–Mo–B amorphous alloy. J Alloy Compd. 2006;407:125–8.
5. Hossain MK, Ferdous J, Haque MM, Abdul Hakim AKM. Development of nanostructure formation of $Fe_{73.5}Cu_1Nb_3Si_{13.5}B_9$ alloy from amorphous state on heat treatment. World J Nano Sci Eng. 2015;5:107–14.
6. Lovas A, Kiss LF, Varga B, Kamasa P, Balogh I, Bakonyi I. Survey of magnetic properties during and after amorphous-nanocrystalline transformation. Journal de Physique. 1998;8:291–8.
7. Inoue A, Wang XM. Bulk amorphous C_{20}(Fe–C–Si) alloys with small amounts of B and their crystallized structure and mechanical properties. Acta Mater. 2000;48:1383–95.
8. Hammam MAS, Abdel-Rahim MA, Hafiz MM, Abu-Sehly AA. New combination of non-isothermal kinetics-revealing methods. J Therm Anal Calorim. 2017;128:1391–405.
9. Lesz S, Kwapuliński P, Nabiałek M, Zackiewicz P, Hawelek L. Thermal stability, crystallization and magnetic properties of Fe–Co-based metallic glasses. J Therm Anal Calorim. 2016;125:1143–9.
10. Avrami M. Kinetics of phase change. II transformation-time relations for random distribution of nuclei. J Chem Phys. 1940;8:212–24.
11. Kissinger HE. Reaction kinetics in thermal analysis. Anal Chem. 1957;29:1702–6.
12. Prajapati SR, Kasyap S, Patel AT, Pratap A. Non-isothermal crystallization kinetics of $Zr_{52}Cu_{18}Ni_{14}Al_{10}Ti_6$ metallic glass. J Therm Anal Calorim. 2015;8:1–13.
13. Stoica M, Li R, Yavari AR, Vaughan G, Eckert J, Steenberge N, Romera DR. Thermal stability and magnetic properties of FeCoB-SiNb bulk metallic glasses. J Alloy Compd. 2010;504:123–8.
14. Jung HY, Stoica M, Seonghoon Y, Kim DH, Eckert J. Crystallization kinetics of $Fe_{76.5-x}C_{6.0}Si_{3.3}B_{5.5}P_{8.7}Cu_x$ ($x = 0$, 0.5, 1 at.%) bulk amorphous alloy. Metall Mater Trans A. 2014;46:2415–21.
15. Piloyan GO, Ryabchikov ID, Novikova OS. Determination of activation energies of chemical reactions by differential thermal analysis. Nature. 1966;212:1229–302.
16. Coats AW, Redfern JP. Kinetic parameters from thermogravimetric data. Nature. 1964;201:68–9.
17. Šesták J. Applicability of DTA to the study of crystallization kinetics of glasses. Phys Chem Glasses. 1974;15:137–40.
18. Ligero RA, Vazques J, Villares P, Jimenez-Garay R. A study of the crystallization kinetics of some Cu–As–Te glasses. J Mater Sci. 1991;26:211–5.
19. Henderson DW. Experimental analysis of non-isothermal transformations involving nucleation and growth. J Therm Anal. 1979;15:325–31.
20. Wang HR, Min GH, Gao YL, Ye YF, Deng YF. Crystallization products of amorphous Zr–Cu–Ni alloy. J Alloy Compd. 2003;354:124–8.
21. Popescu C. Integral method to analyze the kinetics of heterogeneous reactions under non-isothermal conditions a variant on the Ozawa-Flynn-Wall method. Thermochimal Acta. 1996;285:309–23.
22. Pratap A, Lad KN, Rao TLS, Majmudar P, Saxena NS. Kinetics of crystallization of amorphous $Cu_{50}Ti_{50}$ alloy. J Non-Cryst Solids. 2004;345–346:178–81.
23. Flynn JH, Wall LA, Quick A. Direct method for the determination of activation energy from thermogravimetric data. Polym Lett. 1966;4:323–8.
24. Ozawa T. A new method of analyzing thermogravimetric data. Bull Chem Soc Jpn. 1965;38:1881–6.
25. Ozawa T. Kinetics of non-isothermal crystallization. Polymers. 1971;12:150–8.
26. Ranganathan S, Heimendahl MV. The three activation energies with isothermal transformations: applications to metallic glasses. J Mater Sci. 1981;16:2401.